PHOTOCATALYTIC DEGRADATION/ADSORPTION OF CARCINOGENIC AZO DYE DISPERSE RED 176.1 BY NANOCAGE CU_2O AS A DUAL FUNCTION CATALYST ON THE VISIBLE-LIGHT

LEILA NASSAJI -JAHROMI [a], REZA FAZAELI [b], REZA BEHJATMANESH-ARDAKANI [a,c] AND MEHDI TAGHDIRI [a,c]*

[a]*Department of Chemistry, Payame Noor University, PO Box, 19395-3697, Tehran, Iran.*
[b]*Department of Chemical Engineering, Faculty of Engineering, South Tehran Branch, Islamic Azad University, P.O. Box 11365-4435, Tehran, Iran.*
[c]*Research Center of Environmental Chemistry, Payame Noor University, Ardakan, Yazd, Iran.*

ABSTRACT

Refining and disposal of wastewater is an important concern of textile industries due to the presence of carcinogenic azo dyes. The monoazo dye Disperse Red 167.1 (DR167.1) is used in dyeing polyester and cotton fibers. In this study, Cage Cu_2O particles was synthesized by using non-toxic and inexpensive materials as a bi-functional material that can mineralize this pollutant under light irradiation and dark media. The samples were characterized by FESEM, XRD, BET / BJH, FTIR, and DRS techniques. The crystallite size was almost 24.3 nm by the Williamson-Hall. Direct band gap energy was equal to 2.08 eV by Kubelka-Munk. It revealed a greater photocatalytic performance in visible light than UV-C and it absorbed 49% of the dye within 10 minutes in the darkness. The oxidation results indicated that at pH equal to 6.44 without the presence of H_2O_2, 0.75 $mg.L^{-1}$ of cage Cu_2O and of 94 $mg.L^{-1}$ dye concentration yielded 91 % removal and mineralization during 10 min. Removal under the visible light irradiation increased to 93% upon increasing the time to 40 min. as dye concentration rose from 94 to 340 $mg.L^{-1}$, with a slight reduction in the efficiency of the photocatalytic degradation process, the efficiency was obtained as 91%. Koble Corrigan model was found as the best isotherm model. Reaction kinetics followed the pseudo-second order model. Overall, due to its absorption and removal of dyes in a short time, it can be a good candidate for textile wastewater treatment.

Keywords: Band gap, carcinogenic azo dye Disperse Red 176.1, Cu_2O, Equilibrium Isotherms and Kinetics , Photocatalytic degradation.

1. INTRODUCTION

Water purification is one of the most important concerns of the human today. Regarding pollutants, dyes are widely used in textile, paper, rubber, plastic, leather, cosmetics, pharmaceuticals, medicine, and food industries. Organic chemicals are known as one of the carcinogenic substances. Thus, all over the world, finding methods to refine such wastewater is a challenging issue for the sciences and environmental technology. The removal of organic materials via photocatalyst oxidation has been studied by many researchers. Meanwhile, most semiconductors limit the absorption of light to the ultraviolet region due to the high band gap energy. Much research has focused on photocatalytic oxidation technologies of mono and azo dyes on TiO_2. It is well known for the removal of dyes from textile industries. However, the efficiency of the degradation of dyes is limited. Copper oxide nanoparticles act as a visible light active photocatalyst for the removal of organic pollutants with a high degree of mineralization. In fact that is easily oxidized or reduced by the photoinduced charge carriers [1,2]. Modifying the particle size, morphology, surface energies, and electron structure of the electron and hole displacement in a semiconductor could make changes to the specific surface area, surface-to-volume ratio, absorption area, physical and chemical properties, etc. to improve its environmental applications [3]. Copper (I) oxide has a direct bandgap of 2.17 eV and p-type semiconductor [4,5]. under light irradiation in aqueous solutions, it is possible to reduce to copper metal or oxidation to Cu^{+2}, because of the potential for reduction and oxidation of Cu_2O within its band gap energy [6,7]. Highly oxidizing copper (I) oxide nanoparticles are used in the degradation of many types of organic pollutants in wastewater, in the removal of heavy metal ions in photo-reduction [8] and photooxidation [9], as well as solar and photoelectrochemical cells [10]. For this purpose, Cu_2O has been synthesized via different morphologies such as cubes, octahedra, polyhedral, nanowires, nanocage as well as quasi-flowers and hollow structures [11,12] with different abilities of degradation [13]. Cubic Cu_2O Nanoparticles smaller than 100 nm showed absorption of around 490 nm and larger than 200 nm absorption within 515 - 525 nm [14]. Polyhedral Cu_2O decreased the initial methyl orange (MO) concentration by adsorption followed by photocatalytic activity. On the other hand, the cubic nanoparticles did not show absorption (MO), but its photocatalytic activity was higher than that of polyhedral particles which can be due to a lower percentage of oxygen defects (oxygen vacancies) and prevention of the electron and hole recombination [15,16]. The catalytic activity of (110) crystal planes is greater than that of the octahedral (111) crystal planes [17]. Different morphologies of copper(I) oxide gives different products for the oxidation of propene by oxygen. Specifically, the crystalline surfaces of (111) in an octahedral structure, (100) in cubic and (110) rhombic dodecahedra produce acrolein, carbon dioxide, and propylene oxide, respectively [18]. Despite advances in different methods of nanoparticle synthesis, their industrial applications require further attention. When nano-catalysts are used directly, separation of nanoparticles is difficult due to their colloidal properties. Therefore, if the nanocrystals are organized into larger hollow structures, they can provide more space for mass transfer-dependent applications [19]. Nanostructures with a high surface area and low density have been studied as suitable morphologies.

It is necessary to achieve a precise method for controlling size, morphology, crystallinity, and construction units of a hollow structure. There is still a major challenge in facile synthesis methods for producing hollow structures. Further investigations are required on the mechanism of formation and photocatalytic properties of hollow Cu_2O structures. Meanwhile, a higher surface area does not necessarily increase the photocatalytic activity. Hollow structures have mostly a larger surface area compared to other morphologies. The necessary condition for the initiation of activity is to drive light onto the catalyst surface. The reaction will not occur unless the inner hole surface is exposed to irradiation. Despite numerous studies improving the copper (I) oxide properties, further investigation is still required. Accordingly, in this study, we have investigated the formation mechanism and photocatalytic properties of cage Cu_2O nanoparticles and the effect of this specific morphology on the photocatalytic properties on the removal of azoic pollutants DR167.1. In order to enhance the quality and ability for absorption as well as degradation of this carcinogenic organic material, Investigations have been done regarding thermodynamic, kinetic, and structural points of view.

2. EXPERIMENTAL

2.1. Materials

Polyvinyl pyrrolidone($(C_6H_9NO)_n$, (PVP)), Copper (II) sulfate ($CuSO_4 \cdot 5H_2O$), Trisodium citrate ($Na_3C_6H_5O_7$), Sodium carbonate (Na_2CO_3), Glucose($C_6H_{12}O_6$), Ethyl alcohol(EtOH), and DR167.1($C_{22}H_{24}ClN_5O_7$) dyestuff were purchased from Sigma-Aldrich Company. All reactions were carried out under normal conditions and all chemicals were used directly without further purification. The properties and chemical structure of the dye are reported in Tab. 1.

*Corresponding author email: r_fazaeli@azad.ac.ir

Table 1. Chemical structure of the dye

Name	**Disperse red 167.1 (DR176.1)**
CAS Registry Number	**DR 79300-l3-3167.1**
λmax (nm)	**456.5**
Chemical Structures	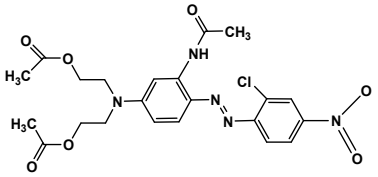
M_W	**505.91**
Formula	**$C_{22}H_{24}ClN_5O_7$**

2.2. Synthesis of Cu_2O nanoparticles

In this study, 0.9 g PVP (K-30, Mw = 30000 g.mol^{-1}) as a cage agent was dissolved in 17 mL DI water. Then, 1 mL of $CuSO_4.5H_2O$ 0.68 mol.L^{-1}, 1 mL of $Na_3C_6H_5O_7$ 0.74 mol.L^{-1}, 1 mL of Na_2CO_3 1.2 mol.L^{-1}, respectively were added dropwise to the first container. Next, 1 mL of glucose 1.4 mol.L^{-1} was added slowly as a reducing agent. Thereafter, it was heated in a 80 °C water bath for 2 h until appearance of orange color and then cooling to room temperature. For 20 days, the colloidal solution was exposed to air. On days 3, 12, 16, and 20, sampling was done. Orange sediment was washed with a mixture of 50 % of the water and alcohol. It was dried in a vacuum oven at 80 °C for 8 h. The color variation of the sample during synthesis has been was shown in Fig. S1 in the Supporting Information.

2.3. Photoreactor

For this purpose, a batch photoreactor was used with a wooden wall. All of the inner walls were covered with aluminum foil to produce the same irradiation in all directions. Xe lamp 400 W was used as a visible submerged light source. Also, to reduce the errors separate and identical samples were considered for each studied time. The schematic view of the photoreactor is displayed in Fig. S2 in the Supporting Information.

2.4. Characterization

The morphology and structure of the synthetic nanoparticles (FESEM) were determined using field emission electron microscopy (TESCAN MIRA3 XMU). The band gap energy calculation was vindicated using the Avantes Avaspec-2048-TEC Spectrophotometer. The absorption spectra were evaluated to calculate the efficiency of the degradation within the range of 260-750 nm. The crystal phase characteristics, crystallite size, and particle size distribution were analyzed by changing different parameters of the synthesized samples via X-ray diffraction using Philips X'Pert Pro X-ray diffraction meter (Netherlands with Kα copper cathode (λ = 1.5406 A˚). FTIR (RX I PerkinElmer, USA) spectra of nanoparticles and dyes were investigated for characterizing and measuring chemical species and for identifying organic compounds. The pore size distribution was calculated using BET and BJH techniques by Japan's Belsorp mini instrument.

3. RESULTS AND DISCUSSION

3.1 XRD analysis

The crystal phase characteristics and crystallite size were investigated by the x-ray diffraction pattern of the synthesized cage Cu_2O, as demonstrated in Fig. 1. A good agreement was observed with JCPDS NO. 01-074-1230. According to the results obtained by XRD interpretation via X'pert Highscore software, the cubic crystal structure (a=4.260 nm, pn-3m space group(224)) was identified; peaks observed at 29.65˚, 36.50˚, 42.40˚, 52.57˚, 61.51˚, 73.71˚ and 77.52˚ corresponded to (110), (111), (200), (211), (220), (311) and (222), crystal faces, respectively. The 3D structure of Cu_2O is displayed in Fig. S3 in the Supporting Information.

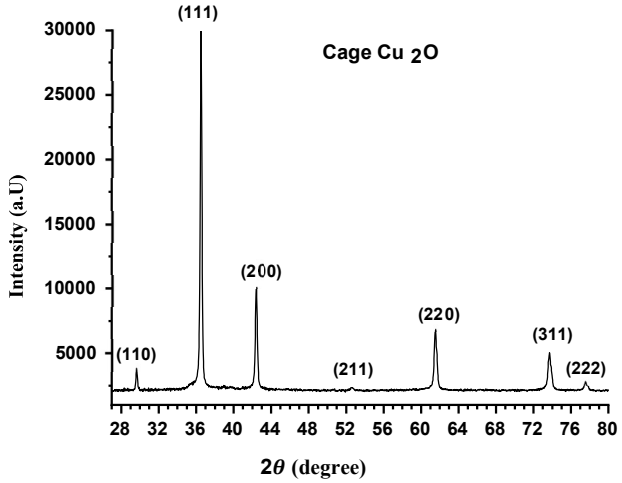

Figure 1. Diffractogram of cage Cu_2O with the related Miller indices for each peak.

The average particle size based on the Williamson-Hall equation (Eq. 1).

$$\beta Cos\theta = \frac{K\lambda}{D} + (4\epsilon)sin\theta \quad (1)$$

Where, β denotes the peak integral width, K is the diffraction vector, $\mathcal{E}$ represents the strain rate of residual, and D is the average crystallite size estimated to be 24.96 nm based on Williamson Hall equation. The average size of the crystals was estimated to be 40.8 based on the Scherrer equation (Eq. S1) $\mathcal{E}$ was equal to -0.0162 which can be a reason for the difference in the results from the two methods.

3.2 FESEM analysis and formation process

Polyhedral nanoparticles were synthesized by adding glucose as a weak reducing agent to the copper citrate complex. They were exposed to oxygen at room temperature for 3, 12, and 16 days. The nanocage Cu_2O was obtained via oxidation at room temperature. The morphology of the synthetic nanoparticles was identified through the field emission scanning electron microscopy (FESEM) analysis.

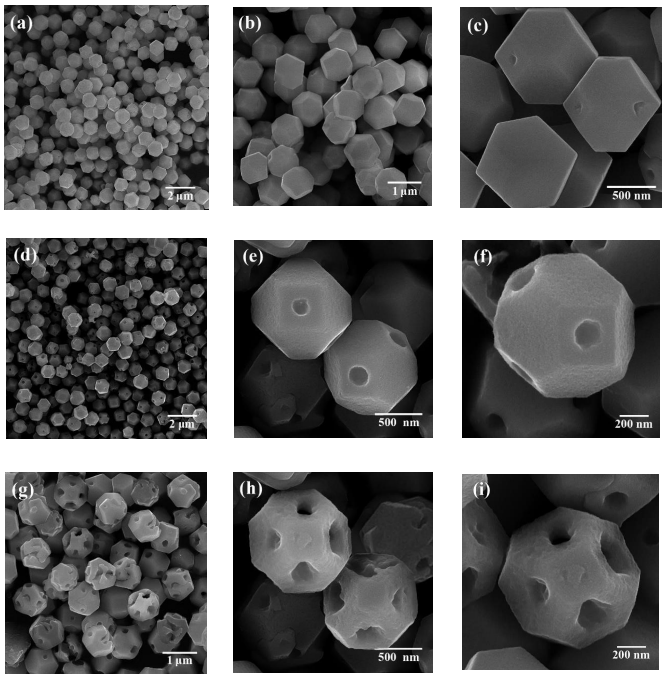

Figure 2. FESEM micrograph of nanocages Cu_2O obtained at room temperature after aging for 3 (a,b,c), 12 (d,e,f)and 16 days (g,h,i).

Fig. 2 indicates highly ordered, uniform, and very regular symmetric nanocage at scales (f,i) 200, (c,e,h) 500 nm, (b,g) 1µm, and (a,d) 2µm. According to the FESEM images, a regular polyhedron structure with an average size of 355 nm was synthesized including hexagonal {111} surfaces and square {100} surfaces (Fig. 2(f)). The size in FESEM to be large compare to crystallite size we have explained this difference in Supporting Infotmation.

Upon oxidation at room temperature, a small pit was created on the square {100} surfaces (Fig. 2(c)). Upon increase in the aging time and gradual oxidation, the diameter of this pits increased while the thickness diminished Fig. 2(d). After more than 16 days of gradual oxidation, the structure was collapsed and fragmented as shown in Fig. 2(g). The presence of oxygen is essential for the formation of hollow structures. By increasing the aging duration, the color of the solution changed from brownish-red to blueish-green, which became similar to the main solution of copper citrate complex. The hollow structures were obtained in equilibrium between two opposing reactions. They reduced copper citrate complex $[Cu_2(cit)_2]^{-2}$ to Cu^+ (Cu_2O) and oxidized Cu^+ to Cu^{2+} corresponding to Eqs. (2,3). Note that it was similar to the synthesis process of nanocage Pb particles [20].

$$2Cu^{2+} + 2\ cit^{-} \rightarrow [Cu_2\ (cit)_2]^{2-} \quad (2)$$

$$2Cu_2O + 4H_2O + O_2 \rightarrow 4Cu^{2+} + 8OH^{-} \quad (3)$$

Copper atoms in { 111 } faces have a free bond to connect. Thus, these are more active in interacting with the PVP. Note that the adsorption of organic material (PVP) on these surfaces blocked them, acting like a protector effectively preventing its oxidation [21]. The average diameter of the hole was 190 nm after 12 days.

3.3 Band gap energy

In this research, to measure the band gap energy, two methodologies were used: Kubelka-Munk and Tauc. The simple analysis of the interaction of light emitted to a thin and isotropic layer of material was done by the KubelkaMunk method [22]. UV-Vis reflectance spectra depend on the parameters such as surface, thickness, scattering factor. and refractive index. F (R) is a function as follows (Eq. 4):

$$F(R) = \frac{(1-R_\infty)^2}{2R_\infty} = \frac{k}{s} \quad (4)$$

(s) and (k) is emission coefficients and absorption, respectively and R_∞ is the ratio of R_{sample} to $R_{standard}$.

The band gap of a thin film of cage Cu_2O with 1-, 3-, 12-, and 16-day aging coated on a quartz substrate was studied by Kubelka-Munk methodology. According to the results, the energy band gap values are 2.12, 2.1, 2.085, and 2.08 eV, respectively. Kubelka-Munk diagram for calculation of cage Cu_2O band gap energy is shown in Fig. 3. Upon increasing the aging time, the reflection spectrum was reduced (Fig. 3(a)) and the energy gap diminished to a little extent (Fig. 3 (b,c,d,e)). In the rest of the study, only the synthesized structure with 12 days of aging was used due to its symmetry and less band gap.

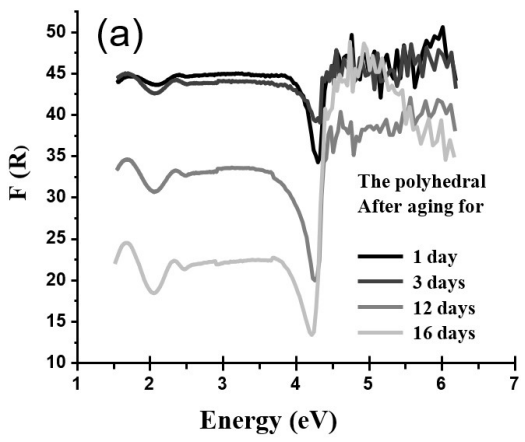

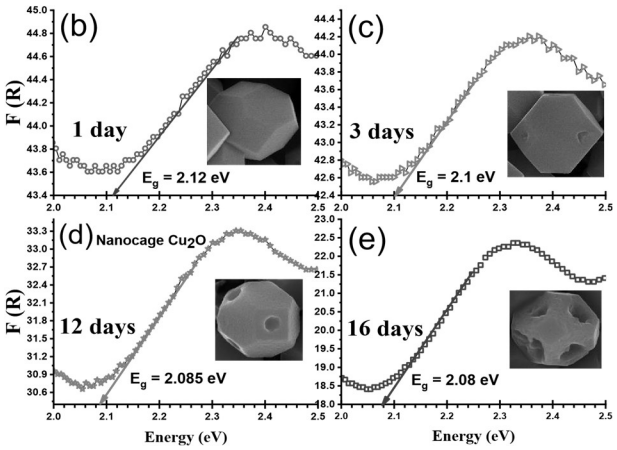

Figure 3. (a) A diagram of Kubelka-Munk to calculate the band gap for copper oxide obtained at room temperature after aging for 1 (b), 3 (c), 12 (d), 16 (e) day(s).

Also, the energy band gap was investigated of Nanocage after aging for 12 days using reflectance spectroscopy (DRS). The results of the direct and indirect allowed band gap were 2.15 and 1.5 eV, respectively. As shown in Fig. S4, the band gap value of direct energy is larger than that of the indirect energy, with both classifying this sample into semiconductor material, which is a significant result.

3.4 BET& BJH analysis

The results of nitrogen adsorption/desorption analysis are reported in Tab. 2 through BET / BJH techniques for Cu_2O. The value of C is obtained from the equation with a dimensionless quantity as follows (Eq. 5):

Table 2. BET/BJH analysis results for Cu_2O.

Shape	a_s , BET [$m^2.g^{-1}$]	a_s , Lang [$m^2.g^{-1}$]	Total pore volume [$cm^3\ g^{-1}$]	Average pore diameter [nm]	a_p [$m^2.g^{-1}$]	V_p [$cm^3.g^{-1}$]	$r_{p,peak}$ (Area) [nm]	C
Nanocage	4.0254	5.5146	0.014268	14.177	4.5728	0.014241	1.66	17.01
[23]	6.15		0.014198	8.6				

a_p: mean pore diameter.
V_m: total absorbed gas.
C: constant related to the energy of adsorption

$$C = exp\frac{(H_1 - H_L)}{RT} \quad (5)$$

H_L represents the heat of liquefication and H_1 denotes the heat of adsorption on the first layer. If H_1 and H_L are equal, the value of C becomes one. This means that there is little difference between adsorption on the surface or adsorption on another layer. On the other hand, if the adsorption in the subsequent layers is weaker than in the surface layer, the value of C will be larger than one. That means the adsorption on the surface layer is more desirable than liquefaction. In our structure, C was 17.01 and the average diameter of its pores was 14.178 nm, which are far higher than the previous research values [23].

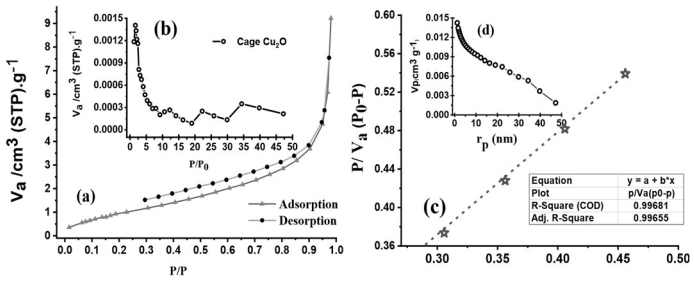

Figure 4. N_2 adsorption-desorption isotherm of the Cage Cu_2O (b) variation of pore volume derivative versus pore radius (c) BET plot (d) variation of pore volume vs.pore radius.

Fig. 4(a) presents the adsorption/desorption isotherm of the nitrogen with the pore size distribution. The type (II)was characterized with type B hysteresis loop. It is caused by non - rigid aggregation of plane particles. The adsorption isotherm was increased curve vertically near P_0 (0.95-1 pressure). It can be attributed to the infinite thickness of the film. Indicates the absorbed capillary density is higher relative pressure. Due to the multilayer adsorption, it occurs in capillary density in the pores. The open cylindrical pores have created the hysteresis loop in the adsorption and desorption curve. The adsorption and desorption curve have a soft slope. It indicates the size variation in similar pore and the different width and neck radius in this morphology. The adsorbate molecules penetrate into the porous adsorbent surface and increase the adsorption.

Fig. 4 (b) depict that by increasing pore necks up to 10 nm, the volume variation of pores is reduced, the volume variations of the pores are irregular to the neck radius with the increase of the pores' neck from 10 to 50 nm.

In Fig. 4 (c) an appropriate linear dependence can be found in the P/P_0 range of 0.3 to 0.5 and indicates good conformity with BET, the correlation coefficient equal to 0.996 indicates it. Fig. 4 (d) indicates that the volume of pores is decreased with the increase of pore radius, meaning that the volume of pores with a larger radius has a smaller value.

3.5 Photocatalytic activity

3.5.1 Photolysis and adsorption effect

The 400 W Xenon visible light was used in photodegradation of DR 167.1 dye in a batch reactor. Specified intervals were considered in order to investigate the stability through visible light irradiation. Fig. S5 (curve b) in the Supporting Information indicates an insignificant dye degradation under photolysis. Under the same darkness conditions, equal amounts of cage Cu_2O were placed in the dye solution, for intervals specific time up to 60 min. After 10 min centrifugation at 12,000 rpm, variations in the dye concentration were traced by UV-Visible spectroscopy. Fig. S5 (curve c) indicates that within the first 10 minutes, approximately 49% was the highest dye adsorption, which increased to 57% at 60 min.

3.5.2 Photodegradation

For reducing instrumental and personal error, identical and separate samples were considered for each specific time in a batch. Equal amounts of cage Cu_2O were placed in the DR167.1 solution with specific concentrations, under visible light irradiation for specific time intervals up to 40 min. At a maximum wavelength of 456.5 nm, measurements were taken measurements on the elimination using the following equation. (Eq. 6), calculating the percentage of degradation or efficiency.

$$\text{Degradation } \% = \left(\frac{C_0 - C_t}{C_0}\right) \times 100 \quad (6)$$

Where C_t presented dye concentration at time t ($mg.L^{-1}$) and C_0 denoted the initial concentration. Fig. 5 indicates the efficiency of degradation was about 85 % for the adsorption variations of 210 $mg.L^{-1}$ of DR167.1 by 1 $g.L^{-1}$ of cage Cu_2O in 40 minutes .

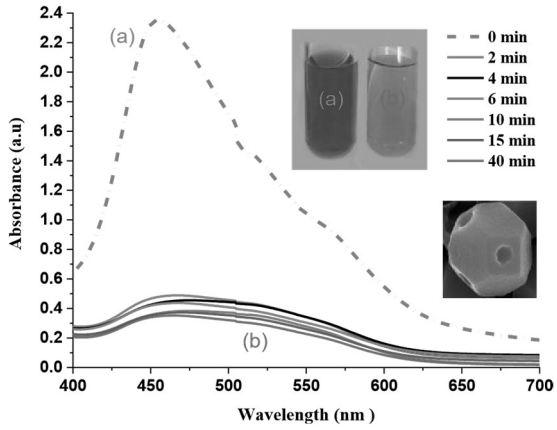

Figure 5. (a) Primary sample (b) degradation of DR167.1 in cage Cu_2O.

The degradation of dyes was accelerated by strong oxidizing agents such as hydroxyl radical (•OH). Hydroxyl radical is produced by several reactions such as hole reaction created during OH^- production. The hydroxyl radical is more active than the free radicals such as $\bullet O_2^-$ and $\bullet HO_2$ that also involved in the process of oxidation. The chemical reactions that cause the photodegradation of the dyes are shown in the equations (7-16) as follows[24]:

Photoexcitation	Photocatalyst $+hv \rightarrow e^-_{CB} + h^+_{VB}$	(7)
Charge carrier trapping of e^-	$e^-_{CB} \rightarrow e^-_{TR}$	(8)
Charge carrier trapping of h^+	$h^+_{VB} \rightarrow h^+_{TR}$	(9)
Electron-hole recombination	$e^-_{TR} + h^+_{VB} (h^+_{TR}) \rightarrow e^-_{CB}$ +heat	(10)
Ionization of water	$H_2O \rightarrow H^+ + OH^-$	(11)
Oxidation of hydroxyls	$OH^- + h^+ \rightarrow {}^{\bullet}OH$	(12)
Oxygen ion-sorption	$(O_2)abs + e^- \rightarrow {}^{\bullet}O_2^-$	(13)
Protonation of superoxide	${}^{\bullet}O_2^- + H^+ \rightarrow {}^{\bullet}HOO$	(14)
Photodegradation by OH^-	$R{-}H + {}^{\bullet}OH \rightarrow {}^{\bullet}R' + H_2O$	(15)
Direct degradation by h^+	$R + h^+ \rightarrow {}^{\bullet}R^+ +$ Intermediates	(16)

As shown in the above reaction, traps such as O_2 and H^+ prevented their recombination by trapping electron and holes.

3.5.3 Irradiation effects

The photocatalytic degradation of dyes by cage Cu_2O was compared under irradiation visible light, UV-C, and in darkness as plotted in Fig. 6 (a). For this purpose, 0.75 $g.L^{-1}$ cage Cu_2O was irradiated with 210 $mg.L^{-1}$ dye for 75 minutes with the changes in the dye concentration being measured by UV-Visible spectroscopy. According to Fig. 6 (b), the percentage of dye degradation was 91%, 61% and 57% under visible light irradiation, UV-C, darkness, respectively.

3.5.4 Adsorption in the absence of light

Besides photocatalytic mineralization of DR167.1, the removal of DR167.1 in under dark condition may have two reasons adsorption and degradation. Degradation of organic contaminants is attributed to the capability of reactive oxygen species (ROS) generation. So, to find out the main reason of DR167.1 removal under dark condition, the dissolved oxygen in DR167.1 solution was eliminated by bubbling with high purity nitrogen gas in a closed sample container. As shown in Fig. 6 (b), the removal efficiency of DR167.1 with Cage Cu_2O under dark condition was significantly decreased after the O_2 elimination, According to Fig. 6 (b), the percentage of dye degradation was 18%, under dark condition in the presence of nitrogen,Which indicating the origin of DR167.1 elimination in the absence of light by cage Cu_2O is related to ROS rather than adsorption. The time-dependent UV–Vis spectra of DR167.1 in Cu_2O suspension /DR167.1 systems under dark and irradiation conditions was shown in Fig. 6 (b). Removal of DR167.1 is affected by •OH and Cu^+ species. The surface of Cage Cu_2O contains rich oxygen vacancies, which can adsorb O_2 Under dark conditions, Cu_2O may be corroded to Cu^{2+} with the reduction of chemisorbed O_2 or make O_2 easier to be reduced to $\bullet O_2^-$ which plays a dominant role in the formation of Cu^+. Therefore, Cage Cu_2O can produce many Cu^+ and affected the azo bond's cleavage and subsequent mineralization in the absence of light irradiation. Some the chemical reactions that cause the removal of the dye in dark conditions are shown in the equations (17-19).

$$Cu^+ (O_V) + O_2 \rightarrow Cu^{2+} \quad (17)$$

$$(O_2)ads + e^- \rightarrow {}^{\bullet}O_2^- \quad (18)$$

$$\bullet O^{2-} + Cu^{2+} \rightarrow Cu^+ + O_2 \quad (19)$$

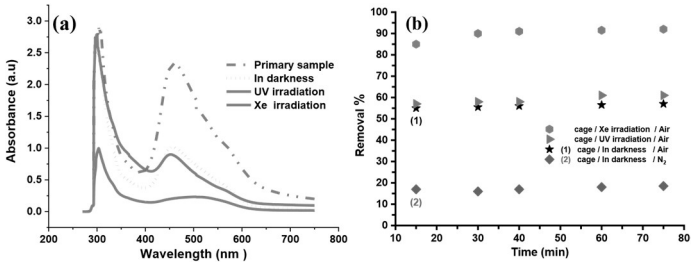

Figure 6. The photocatalytic degradation process of DR167.1 by cage Cu_2O under different light sources; (a) at different wavelengths after 75 minutes, (b) in different times-dependent irradiations (curve c & d) aerobic and anaerobic degradation in darkness.

3.5.5 Photocatalyst dosage

The dye degradation was compared at different concentrations 0.5, 0.75, 1.0, 1.25, 1.5 $g.L^{-1}$ of cage Cu_2O in 50 $mg.L^{-1}$ dye solution, which was investigated at clear intervals up to 40 min. According to Fig. 7, the maximum efficiency was obtained at 0.75 $g.L^{-1}$ concentration of cage Cu_2O.

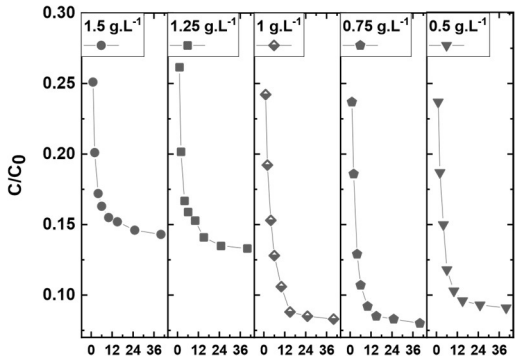

Figure 7. Influence of the cage Cu_2O concentration on the degradation in time-dependent.

The light penetration was reduced by increasing the catalyst concentration from $1gL^{-1}$to 1.25 $g.L^{-1}$ Thus, the electron excitation diminished while the aggregation and clotting of nanoparticles increased; eventually, the rate of the photocatalytic process was reduced [25, 26].

3.5.6 PH effects

For this section, the photocatalytic degradation was investigated at the dye concentration of 340 $mg.L^{-1}$ at solution pHs 4, 5, 5.5, 6.44, 7.44, and 10 for o.75$g.L^{-1}$ cage Cu_2O . Fig. 8 depicts that in the interval of 0 to 2 minutes, the maximum efficiency occurred at pH equal to 6.44. Upon prolongation of the time up to 40 min, at pH 6. 44, 7.44, 5.5, 5.0, 4.0 and 10.0, the photocatalytic degradation rate was found as 87.9%, 84.3%,8 1.7% , 80.92%, 79.05%, and 76.94 %, respectively.

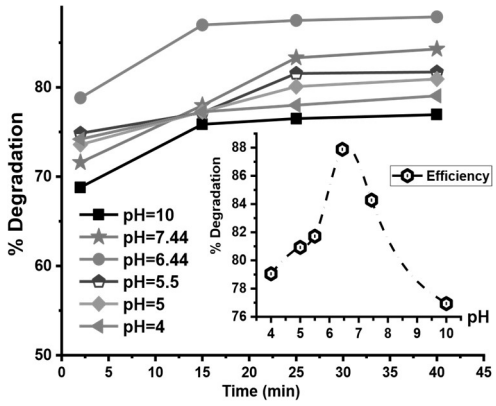

Figure 8. Effect of the initial pH on the photodegradation of DR167.1.

At pH 6.44, the surfaces of the dye and the copper oxide have a positive and negative charge, respectively, caused by copper oxide's pH_{pzc} equal to 5 [27, 28]. This leads to an electrostatic attraction between the dye and catalyst, followed by better adsorption and degradation. Note that it diminishes in the alkaline environment due to the coulomb repulsion of less absorption and degradation [29, 30, 31]. With the increase in the surface area of the catalyst, absorption grows by increasing the number of active sites. Subsequently, the effect of the pH factor increases [32, 33].

3.6. FTIR analysis

3.6.1. FTIR spectrum of cage Cu_2O

In this research, to characterize the molecular structure of the photocatalyst, FTIR spectrum was used. For this purpose, the initial FTIR spectra of DR167.1, cage Cu_2O, and DR167.1/cage Cu_2O were determined after 25 minutes of a photocatalytic process within the range of 400-4000 cm^{-1} (Fig. S6).

Fig. S6 (curve b), reveals the FTIR spectrum of cage Cu_2O in the initial condition. The following peaks were observed: the peaks of 433.8, 448.7, 513.8, 613.8, 778.96, 837.28, 955.31, 1108.94, 1204.16, 1327.71, 1626.56, 2313.21, 2877.65, 3410.38.4, 3739.24, 3933.23 cm^{-1}. Fig. S6(curve c) depict the FTIR spectrum of DR 167.1 / cage Cu_2O, it is clearly evident that the peaks of 1043.37, 1127.49, 1170.68, 1519.03, 1617.03, 1738.71cm^{-1} corresponded to the DR167.1 (Fig. S6(curve a)) absorbed by cage Cu_2O while 833.75, 490.66, 525.56cm^{-1} peaks are associated with dye degradation after light Xe irradiation.

3.6.2 FTIR spectrum of DR 167.1

Fig. S7 displays the FTIR spectra of DR 167.1 dye before and after the photocatalytic degradation process to illustrate the presence of different functional groups.

Fig.S7 (curve A) depicts the FTIR spectrum of DR167.1 in the initial condition. The following peaks were observed: peak at 618.56 cm^{-1} for stretching vibration of –C-N in the ring compounds ,745.73 cm^{-1} for the presence of benzene ring, 8.18.29 cm^{-1} for the stretching vibration of –N-O, 887.4 cm^{-1} due to the presence of C-H in the alkanes,1037.2 cm^{-1} due to the presence of aryl-alkyl in the structure, 1225 and 1118.21 cm^{-1} for the stretching vibrations of –C-N-,1375.13 cm^{-1} for the stretching vibrations of –CH3, 1515.84 and 1615.84 cm^{-1} due to the presence of azo -N = N- group, 1738.68 and 1687.75 cm^{-1} for carbonyl stretching vibrations of -C=O, 2910.33 cm^{-1} for the stretching vibrations of (CO) –H, and 3433.2 plus 3742.29 cm^{-1} for stretching vibrations of –O-H and –N-H, respectively.

Fig. S7 (curve B). After two minutes, an FTIR spectrum was taken from the remaining dye sample after centrifugation. The removal of some peaks or the presence of new peaks suggests a restructuring of the material. In the first two minutes, the azo bond was removed, with the absence of 1515.84 and 1615.84 cm^{-1} peaks confirming it. The following peaks were observed: 831.99 cm^{-1} for the stretching vibration of alkane C-H, 738.24 cm^{-1} for the presence of a ring Benzene , 1120.47 cm^{-1} related to the stretching vibration of –C-N-, 1643.97 cm^{-1} for –C=C, 2313.33 cm^{-1} related to CO_2 [34], 2905.43 cm^{-1} for stretching vibrations of (CO)-H, 3469.57-3802.54 cm^{-1} for the stretching vibrations of O-H and N-H. Peaks 1328.11, 1200.24, 831.99 cm^{-1} were also seen in pure copper oxide spectra which can be attributed to the presence of copper oxide colloidal nanoparticles in the dye solution after centrifugation.

Fig. S7 (curve C). After 25 minutes of the experiment, again an FTIR spectrum was taken from the remaining dye sample. No peak was observed related benzene ring, while the following peaks were observed:

Peak at 833.1cm^{-1} for stretching vibrations of alkane C-H [35], 1123.21cm^{-1} related to the stretching vibrations of –C-N- and C-O-C, 1643cm^{-1} for stretching vibrations of –C=C-, 2313.27cm^{-1} related to CO_2 ,2917.53cm^{-1} for stretching vibrations of (CO)-H and –C-H- and 3736.89 , 3457.96$cm^{-1}$for stretching vibrations of –O-H and –N-H. In pure copper oxide spectra, 1326.71 and 1198.05cm^{-1} peaks were also seen which can be attributed to the presence of colloidal cage Cu_2O in the dye solution after centrifugation. The decline in the peak intensities from (A) to (C) indicates a reduction in the concentration of residual material. Based on the experimental results and Ref. [36,37], a possible path for the photocatalytic degradation of DR 167.1 is presented in Fig. 9.

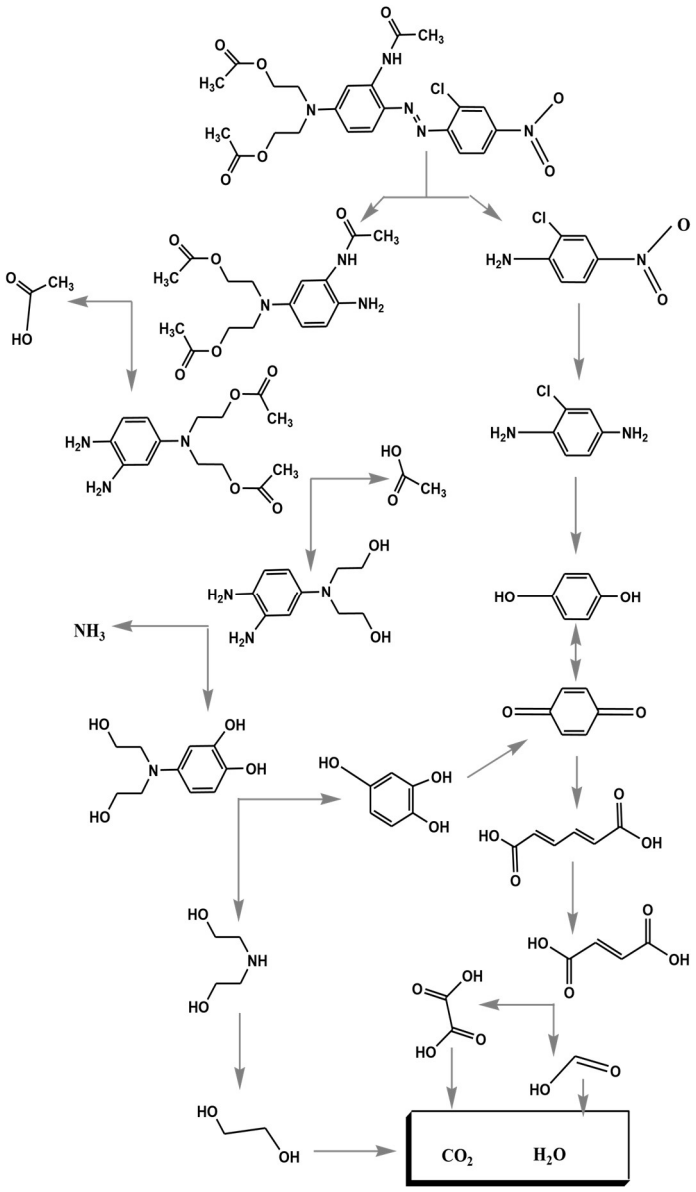

Figure 9. Proposed pathway for degradation of DR167.1 under visible light.

3.7 Adsorption isotherm

Eight experiments were designed for this purpose, with samples containing DR 167.1 dye at different concentrations (50, 94, 155, 196, 208, 245, 290 and 342 mg.L^{-1}) and o.75 g.L^{-1} cage Cu_2O at pH of 6.44 being exposed to Xenon visible light in a photoreactor. The dye concentration was measured at 40 minutes. The equilibrium absorption capacity of the catalyst was obtained from them as follows (Eq. 20).

$$q_e = \frac{(C_0 - C_e)V}{W} \quad (20)$$

Where , C_0 and $C_e$represent the initial and final concentrations (mg.L^{-1}), q_e denotes the mass absorbed per unit mass of the adsorbent (mg.g^{-1}), W is the catalyst value (g), and V reflects the volume of solution (L). Using correlation coefficient (R^2), the thermodynamic behavior of reactions was compared for all isotherm equations. To determine the proper relationship, the functions of Marquardt's percent standard deviation (MPSD) and average relative error (ARE) were used. The error function of (ARE) attempts to reduce the fractional error distribution over the entire concentration range, while the error function (MPSD) is modified according to the number of degrees of freedom of the system [38,39 ,40,41]. The error functions are listed in Tab. 3. Laboratory data were adapted to the isotherm models. Based on the error function minimization, the statistical parameters of these models were evaluated using MATLAB software.

Table 3. Explanation of different error functions.

Abbreviation	Error function	Definition/expression
ARE	Average Relative Error Function	$\frac{100}{n}\sum_{i=1}^{n}\left\|\frac{q_{e,cal}-q_{e,exp}}{q_{e,exp}}\right\|_i$
MPSD	Marquardt's Percent Standard Deviation Error Function	$100\sqrt{\frac{1}{n-p}\sum_{i=1}^{n}\left(\frac{q_{e,exp}-q_{e,cal}}{q_{e,exp}}\right)^2}_i$

Table 4. Nonlinear isotherm equations and Two-, Three- and Four-parameter isotherms along with error functions for photocatalytic degradation of DR 167.1 dye with nanocage Cu_2O nanoparticles.

Isotherm	Nonlinear form	Parameters (units)	Nonlinear isotherm parameter	R^2	ARE %Error	MPSD %Error
Koble-Corrigan	$q_e = \frac{A_{KC}\,C_e^{n_{KC}}}{1 + B_{KC}\,C_e^{n_{KC}}}$	A_{KC}: $(L^n mg^{1-n} g^{-1})$ B_{KC} : $(L/mg)^n$ n_{KC}	47.1343- 0.0001 0.5748	0.9964	3.8997	7.6663
Freundlich	$q_e = k_f . C_e^{1/n}$	K_f : $[mg^{1-n}\,Ln\,g^{-1}]$ n	47.1231 1.73914	0.9964	4.9208	8.8091
Khan	$q_e = \frac{q_{SK} . b_K . C_e}{(1 + b_K . C_e)^{a_K}}$	q_{sK} b_k a_K	1.6269 350.4780 0.4253	0.9964	4.9237	9.6556
Baudu	$q_e = \frac{q_{mB} . b . C_e^{(1+x+y)}}{1 + b . C_e^{(1+x)}}$	q_{mB} : (mg/g) b_0 x y	47.1232 -208.6572 171.1396 0.5750	0.9964	4.7287	10.789
Radke_prausnitz	$q_e = \frac{a_{RP} . r_{RP} . C_e}{1 + r_{RP} . C_e^{B_{RP}}}$	a_{RP} : (L/mg) r_{RP} B_{RP}	44.0668 -8653999.83 0.3393	0.9964	4.9208	10.789
Fritz-Schlunder	$q_e = \frac{C\,C_e^{\alpha_{FS}}}{1 + D_{FS} . C_e^{\beta}}$	C D_{FS} α_{FS} β	45.2083 0.0000008 0.5917 2.7867	0.9965	5.2618	10.796
Jovanovich	$q_e = q_m . (1 - e^{-K_J . C_e})$	q_m :(mg/g) K_j	458.5111 0.0455	0.9883	9.5835	23.082
Tempkin	$q_e = B_T . \ln(A_T . C_e)$	A_T : (L/mg) B_T	0.9774 93.7100	0.9400	14.495	23.055
Redlich_Peterson	$q_e = \frac{K_R . C_e}{1 + a_R . C_e^{g}}$	K_R : (L/g) a_R: (L/mg) g	7.9806 -1.8892 -0.5683	0.9377	4.7482	8.0888
Dubinin_Radushkevich	$q_e = \frac{q_{mB} . b . C_e^{(1+x+y)}}{1 + b . C_e^{(1+x)}}$	q_{SD} K_{ad} :(mol^2/J^2)	356.8792 77.8332	0.9148	22.675	39.775

The isotherms constants, corresponding correlation coefficients, and error function achieved by the nonlinear method, are reported in Tab. 4. According to this table, Koble-Corrigan, Freundlich, and Khan have a maximum correlation factor. It is also observed that the Koble-Corrigan has had lower error function values indicating better accuracy of this model. The error value by ARE was 3.899, 4.920, and 4.923, while by MPSD it was 7.66, 8.80, and 9.65 respectively.

3.8 Adsorption kinetic

To better understand the process, the kinetics of the process were investigated. To this end, The samples containing DR167.1 with different concentrations (94, 155, 196, 208, 245, 290, and 342 ppm) with 0.75 g.L^{-1} of cage Cu_2O at pH of 6.44 were exposed to visible light for 40 minutes. At specified time intervals, the variations of sample concentrations were measured; where q_t is the mass absorbed per unit mass of the adsorbent at time (mg.g^{-1}) and is calculated from Eq. (21). The kinetic models are presented in Tab. 5.

$$q_t = \frac{(C_0 - C_t)V}{W} \quad (21)$$

Table 5. Kinetic models.

Kinetic model	General Formula	Ref.
Langmuir–Hinshelwood	$\frac{1}{K} = \frac{1}{K_{add}^{app} K_{L.H}} + \frac{C_0}{K_{L.H}}$	**[37],[42]**
pseudo first order (Logergern)	$\ln(q_e - q_t) = ln q_e - k_1 t$	**[43],[441],[45]**
pseudo-first-order (Elovich)	$q_t = \frac{1}{\beta}\ln(\alpha\beta) + \frac{1}{\beta}\ln(t)$	**[46],[47]**
Pseudo second order (Blanchard)	$\frac{t}{q_t} = \frac{1}{K_2 q_e^2} + \frac{t}{q_e}$	**[48],[49],[50],[51],[520]**
Intra Particle diffusion control	$q_t = k_i t^{1/2} + C_i$	**[53],[54]**

Table 6. Calculation of LH parameters for photodegradation reaction.

	Langmuir–Hinshelwood		
Cage Cu_2O	R^2	$K_{L.H}$	K_{add}^{app}
	0.8605	24.218	0.0019

Table 7. Correlation coefficient for different kinetic models at dye different concentrations.

	Dye (mg/L)	pseudo first order		Pseudo second order Blanchard	Intra Particle diffusion control
		Logergern R^2	Elovich R^2	R^2	R^2
cage Cu_2O	94	*0.7137*	*0.9722*	*0.9997*	**0.8468**
	155	*0.594*	*0.9077*	*0.9999*	**0.7122**
	196	*0.5207*	*0.9899*	*0.9998*	**0.9341**
	208	*0.591*	*0.9771*	*0.9998*	**0.8568**
	245	*0.5825*	*0.9679*	*0.9998*	**0.81**
	290	*0.4388*	*0.9299*	*0.9997*	**0.7819**
	342	*0.4976*	*0.9479*	*0.9994*	**0.8952**

Table 8. Constants and correlation coefficient for Blanchard kinetic model.

	Dye (mg/L)	$(q_e)_{exp}$	Pseudo second order Blanchard		
			K_2	$(q_e)_{cal}$	R^2
cage Cu_2O	94	*117.1160*	*0.019013158*	*117.6471*	**0.9997**
	155	*190.6890*	*0.015905882*	*192.3077*	**0.9999**
	196	*239.7210*	*0.0126*	*238.0952*	**0.9998**
	208	*252.9620*	*0.00950625*	*256.4103*	**0.9998**
	245	*296.5640*	*0.008892308*	*294.1176*	**0.9998**
	290	*342.3120*	*0.00841*	*344.8276*	**0.9997**
	342	*401.2870*	*0.005208333*	*400*	**0.9994**

Since the Blanchard model has the highest correlation coefficient, the adsorption follows the pseudo-second-order equation. These results can be seen in Tab.s 6 and 7. As the dye increased concentration from 94 to 340 mg.L^{-1} for 0.75g.L^{-1} copper (I) oxide, the slope (K_2) revealed a slight descending trendline (Tab. 8). Minor reduction in the efficiency of the photocatalytic degradation process was observed with acceptable efficiency (Fig. 10). Furthermore, the closeness $(q_e)_{cal}$ and $(q_e)_{exp}$ values at all concentrations suggests high accuracy of the experiment (Tab. 8).

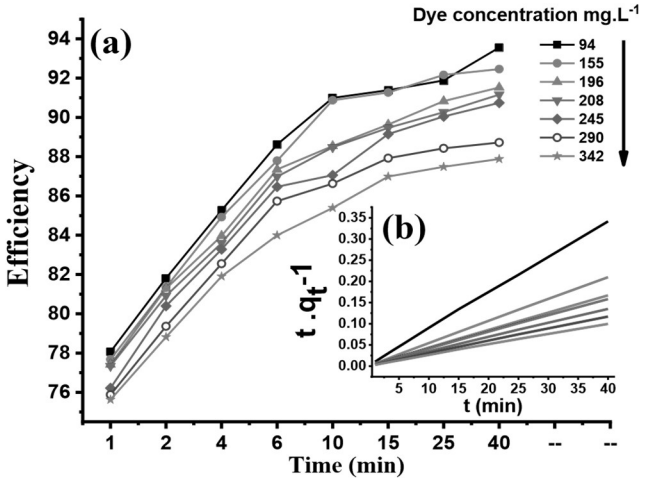

Fig. 10. Influence of the dye concentration on the degradation.

CONCLUSION

In summary, Cage Cu_2O particles was synthesized by using non-toxic and inexpensive materials as a bi-functional material that can degrade contaminants under both light irradiation and dark circumstance. during two stages, the cage Cu_2O was synthesized first via polyhedral formation followed by gradual oxidation at room temperature via co-precipitation in water as a solvent for 3, 12, and 16 days. The presence of PVP and oxygen is necessary for the formation of this morphology. Nonocage for 12 days aging was obtained as highly ordered, uniform, and very regularly symmetrical. The effect of this material as a photocatalyst was investigated on the removal of DR167.1 carcinogenic dye under visible xenon light without the presence of excess oxidant (H_2O_2). From an isothermic point of view, the highest correlations and minimum error values belonged to the Koble Corrigan, Freundlich, and Khan isotherms, respectively. The kinetics of this process followed the pseudo-second-order model. It was shown the efficiency of synthetic photocatalyst in visible in comparison with UV-C irradiation. Removal under the visible light irradiation increased to 93% upon prolongation of time to 40 min. Another possible option to achieve a higher efficiency is adding a suitable dopant to, which is going to be undertaken by our research team.

NOMENCLATURE

Table 9. Values of parameters and Greek letters

Symbols used		
a_K	[-]	Khan isotherm model exponent
a_{RP}	[L.mg^{-1}]	Redlich-Peterson isotherm constant
A_{KC}	(L^{n}mg^{1-n} g^{-1}]	Koble-Corrigan constant
AT	[L.mg^{-1}]	Temkin equilibrium binding
b_K	[-]	Khan constant
b_0	[-]	Baudu equilibrium constant
B_{KC}	[L.mg^{-1}]	Koble-Corrigan isotherm constant
B_T	[-]	Temkin constant
C	[-]	Fritz-Schlunder (IV) constant
C_e	[mg.L^{-1}]	equilibrium concentration of adsorbate
C_0	[mg.L^{-1}]	adsorbate initial concentration
D_{FS}	[-]	Fritz-Schlunder (IV) constant
f	[-]	interaction coefficient of the Frumkin model
g	[-]	Redlich-Peterson isotherm exponent
f	[-]	interaction coefficient of the Frumkin model
k_f	[mg^{1-n} L^n g^{-1}]	Freundlich isotherm constant
K_{ad}	[mol^2.J^{-2}]	Dubinin-Radushkevich isotherm constant related to adsorption energy
K_F	[-]	Frumkin equilibrium constant
Kj	[L.mg^{-1}]	Jovanovich constant
K_R	[L.g^{-1}]	Redlich-Peterson isotherm constant
n	[-]	degree of freedom
n_{KC}	[-]	Koble-Corrigan model exponent
p	[-]	number of isotherm parameters
q_e	[mg.g^{-1}]	equilibrium adsorption capacity of adsorbent
$q_{e,\,cal}$	[mg.g^{-1}]	theoretical equilibrium adsorption capacity of adsorbent
$q_{e,\,exp}$	[mg.g^{-1}]	experimental equilibrium adsorption capacity of adsorbent
q_{mB}	[mg.g^{-1}]	Baudu maximum adsorption capacity
q_{mJ}	[mg.g^{-1}]	Jovanovich maximum adsorption capacity
q_{SD}	[mg.g^{-1}]	Dubinin-Radushkevich theoretical isotherm saturation capacity
q_{SK}	[mg.g^{-1}]	Khan theoretical isotherm saturation capacity
V	[L]	volume of adsorbate solution
W	[g]	mass of adsorbent
x	[-]	Baudu model exponent
y	[-]	Baudu model exponent
Greek letters		
α_{FS}	[-]	Fritz-Schlunder (IV) model exponent
β	[-]	Fritz-Schlunder (IV) model exponent
ε	[-]	Polanyi potential constant related to Dubinin-Radushkev ich model
θ	[-]	coverage degree of adsorbent surface
Abbreviations		
FESEM		Field Emission Scanning Electron Microscope
FTIR		Fourier-transform infrared spectroscopy
FWHM		Full-width-at- half-maximum
XRD		X-ray diffraction

ACKNOWLEDGMENTS

Part of the cost of this research was supported by the financial grants from Payame Noor University of Ardakan. We would like to appreciate Dr. Seyed Ali Pourmosavi (Deputy of Education and Graduate Education, Damghan University in Iran) and Dr. Ghazaleh Chizari Fard for their guidance in this research.

COMPLIANCE WITH ETHICAL STANDARDS

Conflict of Interest: The authors declare that there is no conflict of interest.

SUPPORTING INFORMATION

Supporting Information for this article can be found under https://jcchems.com/index.php/JCCHEMS/article/view/1473/433. This section includes additional references to primary literature relevant for this research.

REFERENCES

1. D. Zhang. Acta Chimica Slovaca 6(1), 141-149, (2013). DOI: 10.2478/acs-2013-0022.
2. Z. Zeng, Y.Yan, , J. Chen, , P. Zan, , Q. Tian, P. Chen. Adv. Funct. Mater, 29(2), 1806500, (2019). DOI: 10.1002/adfm.201806500.
3. Mohamed. R. M, Aazam. E. S. Appl Catal A Gen, 480, 100-107,(2014). DOI: 10.1016/j.apcata.2014.04.039.
4. H. D. Aghdam, H. Azadi, M. Esmaeilzadeh, S. M. Bellah, and R. Malekfar. Optical Materials, 91, 433-438, (2019). DOI: 10.1016/j.optmat.2019.03.027.
5. G.R. Surikanti, A.K. Bandarapu, M.V. Sunkara, ChemistrySelect, 4(8), 2249-2257,(2019). DOI: 10.1002/slct.201900003.
6. G. Wang, R. van den Berg, C. de Mello Donega, K.P. de Jong, P.E. de Jongh, P. E. Appl Catal,B, 192, 199-207, (2016). DOI: 10.1021/jp111778g.
7. Y. Jiang, H.Yuan, H. Chen, ChemPhysChem, 17(1), 630-637,(2015). DOI: 10.1039/C4CP03631J.
8. M. Iqbal, Y. Wang, H. Hu, M. He, A.H. Shah, L. Lin, P. Li, K. Shao, A.R. Woldu, T. He. Appl Surf Sci, 443, 209-216,(2018). DOI: 10.1016/j.apsusc.2018.02.162.
9. B. White, M. Yin, A. Hall, D. Le, S. Stolbov, T. Rahman, N. Turro, S. O'Brien. Nano let, 6(9), 2095-2098, (2006). DOI: 10.1021/nl061457v.
10. B. Wang, W. Zhang, Z. Zhang, R. Li, Y. Wu, Z. Hu, X. Wu, C. Guo, G. Cheng, R. Zheng. RSC advances, 6(105), 103700-103706,(2016). DOI: 10.1039/C6RA22474A.
11. Q. Guo, Y. Li, W. Zeng. Physica E Low Dimens Syst Nanostruct, 114, 113564,(2019). DOI: 10.1016/j.physe.2019.113564 .
12. R. Ji, W. Sun, Y. Chu. ChemPhysChem, 14(17), 3971-3976,(2013). DOI: 10.1002/cphc.201300735.
13. T. Aditya, J. Jana, N.K. Singh, A. Pal, T. Pal. ACS omega, 2(5), 1968-1984, (2017). DOI: 10.1021/acsomega.6b00447.
14. C.H. Kuo, C.H. Chen, M.H. Huang. Adv Funct Mater, 17(18), 3773-3780,(2007). DOI: 10.1002/adfm.200700356.
15. F. Plascencia-Hernández, A.L. Luna, C. Colbeau-Justin, P. Santiago, Garcia-Rocha, M., Valverde-Aguilar, G. M. A.Valenzuela. J. Saudi Chem. Soc, 23(8), 1016-1023,(2019). DOI: 10.1016/j.jscs.2019.05.007.
16. R. Yang, X. Lu, X. Huang, Z. Chen, X. Zhang, M. Xu, Q. Song, L. Zhu. Appl Catal B, 170, 225-232,(2015). DOI: 10.1016/j.apcatb.2015.01.046
17. K. Chanda, S. Rej, M. H. Huang. Chem: Eur. J, 19(47), 16036-16043,(2013). DOI: 10.1002/chem.201302065.
18. Q. Hua, T. Cao, X. K. Gu, J. Lu, Z. Jiang, X. Pan, L. Luo, W.X. Li, W. Huang. Angew Chem Int Ed Engl, 53(19), 4856-4861,(2014). DOI: 10.1002/anie.201402374.
19. H. Zhang, Q. Zhu, Y. Zhang, Y. Wang, L. Zhao, B. Yu. Adv Funct Mater, 17(15), 2766-2771,(2007). DOI: 10.1002/adfm.200601146.
20. Y. Xiong, B. Wiley, J. Chen, Z. Y. Li, Y. Yin, Y. Xia. Angew Chem Int Ed Engl, 44(48), 7913-7917,(2005). DOI: 10.1002/anie.200502722.
21. D. F. Zhang, H. Zhang, L. Guo, K. Zheng, X. D. Han, Z. Zhang. J Mater Chem, 19(29), 5220-5225,(2009). DOI: 10.1039/b816349a.
22. Z. Gao, B. Yao, T. Xu . Techno, 1:1-1,(2019). DOI: 10.1080 /09593330.2019.1670268.
23. W. Janusz, A. GAŁGAN, and M. RESZKA. PHYSICOCHEM PROBL MI, 40, 161-174,(2006).
24. N. I. C. K. Serpone, D. A. R. R. E. N. Lawless, R. Khairutdinov, E. Pelizzetti . J Phys Chem, 99(45), 16655-16661,(1995). DOI: 10.1021/j100045a027.
25. N. Daneshvar, D. Salari, and A. R. Khataee. J. Phys. Chem, 162(2-3), 317-322,(2004). DOI: 10.1016/S1010-6030(03)00378-2.
26. T. Sauer, G. C. Neto, H. J. Jose, R. F. P. M. Moreira. Photobiol. A, 149(1-3), 147-154,(2002). DOI: 10.1016/S1010-6030(02)00015-1
27. M. Kosmulsk. Adv Colloid Interface Sci, 152(1-2), 14-25,(2009). DOI: 10.1016/j.cis.2009.08.003.
28. M. Kosmulsk, CRC pressm(145), 2009.
29. I. K. Konstantinou, T. A. Albanis. Appl Catal B, 49(1), 1-14,(2004). DOI: 10.1016/j.apcatb.2003.11.010.
30. E. Bizani, K. Fytianos, I. Poulios, V. Tsiridis. J. Hazard. Mater, 10;136(1):85-94,(2006). DOI: 10.1016/j.jhazmat.2005.11.017.
31. K. Tanaka, K. Padermpole, T. Hisanaga . Water Res, 34(1), 327-333,(2000). DOI: 10.1016/S0043-1354(99)00093-7.
32. C. Zhu, L. Wang, L. Kong, X. Yang, L. Wang, S. Zheng, H. Zong. Chemosphere, 41(3), 303-309,(2000). DOI: 10.1016/s0045-6535(99)00487-7.
33. C. Hu, C. Y. Jimmy, Z. Hao, P. K. Wong. Appl Catal B, 46(1), 35-47,(2003). DOI: 10.1016/S0926-3373(03)00139-5.
34. S. Maensiri, C. Masingboon, V. Promarak, and S. Seraphin. Opt Mater (Amst), 29(12), 1700-1705,(2007). DOI: 10.1016/j.optmat.2006.09.011
35. D. Bhatia, R. Kanwar, and J. Singh. dspace.lpu.in, 2018. DOI: 10.1016/j.jhazmat.2005.11.017.
36. F. Zhang, G. Dong , M. Wang, Y. Zeng, C. Wang. Appl. Surf. Sci,30,444,559-68,(2018). DOI: 10.1016/j.apsusc.2018.03.087.
37. S. Karthikeyan, S. Kumar, LJ. Durndell, MA. Isaacs, CM. Parlett, B. Coulson, RE. Douthwaite, Z. Jiang, K. Wilson, AF. Lee. ChemCatChem, 21,10(16),3554-63,(2018). DOI:10.1002/cctc.201800439.
38. R. Saadi, Z. Saadi, R. Fazaeli, and N. E. Fard. Korean J Chem Eng, 32(5), 787-799,(2015). DOI: 10.1007/s11814-015-0053-7.
39. J. F. Porter, G. McKay, and K. H. Choy. Chem Eng Sci, 54(24), 5863-5885,(1999). DOI: 10.1016/S0009-2509(99)00178-5.
40. L. Nassaji-Jahromi, R. Fazaeli, R. Behjatmanesh-Ardakani, M.Taghdiri. J. Photochem. Photobiol. A, 392, 112425,(2020). DOI: 10.1016/j.jphotochem.2020.112425.
41. A. Seidel, D. Gelbin. Chem Eng Sci, 43(1), 79-88,(1988). DOI: 10.1016/0009-2509(88)87128-8.
42. S. Agarwal, I. Tyagi, V. K. Gupta, F. Golbaz, A. N. Golikand, O. Moradi. J Mol Liq, 218, 494-498,(2016). DOI: 10.1016/j.molliq.2016.02.040.
43. R. Bazargan-Lari, H. R. Zafarani, M. E. Bahrololoom, and A. Nemati. J Taiwan Inst Chem Eng, 45(4), 1642-1648,(2014). DOI: 10.1016/j.jtice.2013.11.009.
44. B. H. Hameed. J Hazard Mater, 162(2-3), 939-944,(2009). DOI: 10.1016/S0032-9592(02)00239-X.
45. A. Khaled, A. El Nemr, A. El-Sikaily, O. Abdelwahab. Desalination, 238(1-3), 210-232,(2009). DOI: 10.1016/j.desal.2008.02.014.
46. M. Özacar, İ. A. Şengil, H. Türkmenler. Chem Eng J, 143(1-3), 32-42,(2008). DOI: 10.1016/j.cej.2007.12.005.
47. A. Almasian, M. Parvinzadeh Gashti, M. E. Olya, G. Chizari Fard. Desalin Water Treat, 57(44), 20837-20855,(2016). DOI: 10.1080/19443994.2015.1112841.
48. Y. S. Ho, G. McKay. Water Res, 34(3), 735-742,(2000). DOI: 10.1016/S0043-1354(99)00232-8.
49. Y. S. Ho, G. McKay.Process Biochem, 38(7), 1047-1061,(2003). DOI: 10.1016/S0032-9592(02)00239-X.
50. S. Schiewer, A. Balaria. Chem Eng J, 146(2), 211-219,(2009). DOI: 10.1016/j.cej.2008.05.034.
51. S. Vafakhah, M. E. Bahrololoom, and M. Saeedikhani. J Water Resour Prot, 8(13), 1238-1250,(2016). DOI: 10.4236/jwarp.2016.813095.
52. H. I. Chieng, L. B. Lim, N. Priyantha. Environ. Technol, 36(1), 86-97,(2015). DOI: 10.1080/09593330.2014.938124.
53. X. Xiao, D. Liu, Y. Yan, Z. Wu, Z. Wu, G. Cravotto. J Taiwan Inst Chem Eng, 53, 160-167,(2015). DOI: 10.1016/j.jtice.2015.02.031.
54. G. C. Fard, M. Mirjalili, F. Najafi. J Taiwan Inst Chem Eng, 70, 188-199,(2017). DOI: 10.1016/j.jtice.2016.10.045.